

RESEARCH ARTICLE

10.1002/2015JA021526

Key Points:

- The paper concerns ULF wave properties under quasi-radial IMF
- Global hybrid-Vlasov simulation results agree with known foreshock properties and observations
- We suggest a mechanism for oblique wave propagation based on spatial variation of back streaming ions

Supporting Information:

- Movie S1
- Movie S2
- Captions for Movies S1 and S2

Correspondence to:

M. Palmroth,
minna.palmroth@fmi.fi

Citation:

Palmroth, M., et al. (2015), ULF foreshock under radial IMF: THEMIS observations and global kinetic simulation Vlasiator results compared, *J. Geophys. Res. Space Physics*, 120, doi:10.1002/2015JA021526.

Received 3 JUN 2015

Accepted 8 OCT 2015

Accepted article online 13 OCT 2015

ULF foreshock under radial IMF: THEMIS observations and global kinetic simulation Vlasiator results compared

M. Palmroth¹, M. Archer^{2,3}, R. Vainio⁴, H. Hietala², Y. Pfau-Kempf^{1,5}, S. Hoilijoki^{1,5}, O. Hannuksela^{1,5}, U. Ganse⁵, A. Sandroos¹, S. von Alfthan⁶, and J. P. Eastwood²

¹Finnish Meteorological Institute, Helsinki, Finland, ²Blackett Laboratory, Imperial College London, London, UK, ³School of Physics and Astronomy, Queen Mary University of London, London, UK, ⁴Space Research Laboratory, University of Turku, Turku, Finland, ⁵Department of Physics, University of Helsinki, Helsinki, Finland, ⁶CSC-IT Center for Science, Espoo, Finland

Abstract For decades, monochromatic large-scale ultralow frequency (ULF) waves with a period of about 30 s have been observed upstream of the quasi-parallel bow shock. These waves typically propagate obliquely with respect to the interplanetary magnetic field (IMF), while the growth rate for the instability causing the waves is maximized parallel to the magnetic field. It has been suggested that the mechanism for the oblique propagation concerns wave refraction due to the spatial variability of the suprathermal ions, originating from the $\mathbf{E} \times \mathbf{B}$ drift component. We investigate the ULF foreshock under a quasi-radial IMF with Vlasiator, which is a newly developed global hybrid-Vlasov simulation solving the Vlasov equation for protons, while electrons are treated as a charge-neutralizing fluid. We observe the generation of the 30 s ULF waves and compare their properties to previous literature and multipoint Time History of Events and Macroscale Interactions during Substorms (THEMIS) spacecraft observations. We find that Vlasiator reproduces the foreshock ULF waves in all reported observational aspects. We conclude that the variability of the density and velocity of the reflected back streaming ions determines the large-scale structure of the foreshock, which affects the wave frequency, wavelength, and oblique propagation. We conclude that the wave refraction may also be at work for radial IMF conditions, which has earlier been thought of as an exception to the refraction mechanism due to the small $\mathbf{E} \times \mathbf{B}$ drift component. We suggest that additional refraction may be caused by the large-scale spatial variability of the density and velocity of the back streaming ions.

1. Introduction

The interplanetary magnetic field (IMF) divides the Earth's bow shock into roughly two regions according to whether the angle between the bow shock normal and the IMF (θ_{Bn}) is more or less than 45° . In the former (latter) case, the shock is called quasi-perpendicular (quasi-parallel). At the quasi-parallel shock, solar wind particles streaming toward the bow shock can reflect at the shock surface and stream back upstream along the IMF, forming a foreshock. The foreshock exhibits several kinds of waves and wave packets, for example, 1 Hz waves, 3 s waves, sinusoidal and nearly sinusoidal 30 s waves, and shocklets and discrete wave packets [e.g., Hoppe et al., 1981; Russell and Hoppe, 1983; Russell et al., 1987; Greenstadt et al., 1995].

Paschmann et al. [1980] investigated the ion distribution functions within the foreshock and explained the energies of the back streaming particles with a model that depends on the angles between the IMF, bow shock normal, and the solar wind, and compared to 18 events observed by the ISEE spacecraft. Using two-dimensional ISEE spacecraft data, Paschmann et al. [1981] characterized and named a number of different ion distributions in the foreshock. They noted that the reflected populations have a fast beam well separated from the solar wind core population and have a strong temperature anisotropy. On the other hand, Paschmann et al. [1981] characterized diffuse populations occupying a larger area in the phase space, where solar wind core population can be encapsulated by the diffuse ions. In between these two population types, Paschmann et al. [1981] observed transitions of intermediate populations, which led them to suggest that diffuse populations result from pitch angle scattering of the reflected beam populations.

In the category of large-amplitude 30 s waves, both left-handed and right-handed polarizations with similar frequencies and wavelengths have been observed [Hoppe et al., 1981]. The left-handed waves are thought

to originate from ion/ion beam instabilities, while the right-handed polarized waves may be caused by nonresonant firehose instability or by left-handed Alfvén/ion resonant instability [Gary, 1993]. Russell *et al.* [1987] investigated the foreshock waves using two spacecraft and found that the wave characteristics depend on where in the foreshock they are detected. The properties of the left-handed nearly sinusoidal waves are more monochromatic and more weakly compressive closer to the ion foreshock boundary [Sibeck *et al.*, 2008] (later called the foreshock compressional boundary) [Omid *et al.*, 2009; Rojas-Castillo *et al.*, 2013], while deeper in the foreshock they become more compressional and can steepen into shocklets [Greenstadt *et al.*, 1995; Hoppe and Russell, 1983]. This paper concentrates on the quasi-monochromatic left-handed 30 s ultralow frequency (ULF) waves, thought to be due to the right-hand resonant ion-ion beam instability [Gary, 1993] arising from the back streaming ion interaction with the solar wind population.

The 30 s waves were first observed by Greenstadt *et al.* [1968] and Fairfield [1969], and their characteristics have since been the subject of many studies. Although they are called the 30 s waves for their period, a considerable spread in the period has been observed, ranging from 10 s to ~ 55 s [Eastwood *et al.*, 2005a]. The period depends on the IMF strength and cone angle [Takahashi *et al.*, 1984] that ranges from radial IMF (0°) to the typical Parker spiral condition (45°) and beyond. The waves are right-handed in the plasma frame and elliptically polarized [Le and Russell, 1994]. The wavelength is of the order of an Earth radius (R_E) parallel to magnetic field [Le and Russell, 1994], while in the perpendicular direction the wave size can be 8–18 R_E [Archer *et al.*, 2005]. The distribution functions associated with the waves show often either a narrow field-aligned beam (closer to the foreshock compressional boundary), whereas otherwise the distributions are mostly observed as intermediate, diffuse, or gyrophase bunched [Fuselier *et al.*, 1986; Meziane *et al.*, 2001; Mazelle *et al.*, 2003; Kempf *et al.*, 2015].

One intriguing factor related to the 30 s waves is that while the growth rate of the instability giving rise to the waves maximizes in the direction parallel to the ambient magnetic field [Gary, 1993], the waves are observed to propagate obliquely, typically at about 20° with respect to the background magnetic field [Le and Russell, 1994; Eastwood *et al.*, 2005b; Hsieh and Shue, 2013]. Eastwood *et al.* [2004] showed that the wave deflection occurs in the plane defined by the magnetic field and the solar wind velocity direction. Several attempts exist to explain the oblique propagation: Winske *et al.* [1985] proposed that the right-hand resonant instability due to gyrating ions is an important mechanism for wave growth near the bow shock, while Omid *et al.* [1994] and Killen *et al.* [1995] showed that the beam-ring ion distributions may excite oblique waves. Hada *et al.* [1987] proposed a mechanism for the oblique propagation based on refraction. In their mechanism, waves are generated parallel to the magnetic field by instabilities due to the presence of the back streaming ions. As the waves are advected downstream with the solar wind, they may encounter a nonuniform refractive index due to the spatial variation of the back streaming ions. To be refracted, waves need to have a wave vector and a group velocity component along the gradient of the refractive index. For nonzero cone angles, the $\mathbf{E} \times \mathbf{B}$ drift of the beam ions leads to variations in the beam structure that are not aligned with the field and solar wind advection transports the wave across the structured beam. Therefore, refraction of waves initially generated in the parallel direction should occur. However, under radial IMF conditions the group velocity of parallel-propagating waves is along the field lines. If the structure of the beam varies across the field only due to the $\mathbf{E} \times \mathbf{B}$ drift, oblique waves would be present only for nonzero cone angles. Several observations state the opposite, and oblique propagation occurs even under quasi-radial IMF [Eastwood *et al.*, 2005b; Hsieh and Shue, 2013], suggesting the oblique wave propagation is still not fully understood. Observations indicate that the waves bend in many directions, while the oblique propagation angle is not correlated with the wave frequency or polarization, the strength of the IMF, or the solar wind speed [Eastwood *et al.*, 2005b; Hsieh and Shue, 2013].

Modeling the foreshock requires a simulation representing kinetic physics. With limited computational resources in the past, local simulations have therefore prevailed [e.g., Winske, 1985], while the global features of the shock have been out of reach to magnetohydrodynamic simulations [e.g., Janhunen *et al.*, 2012] due to insufficient ion-scale physics. Only during the past decade, computational resources have increased such that it has been possible to investigate the global features of the foreshock. The most common way to model the foreshock is by hybrid particle-in-cell methods (hybrid-PIC), where ions are particles launched to the simulation, while electrons are modeled as a charge-neutralizing fluid [Omid *et al.*, 2005; Blanco-Cano *et al.*, 2006; , 2009; Karimabadi *et al.*, 2014]. These simulations have typically modeled two-dimensional setups

Table 1. Solar Wind and IMF Parameters for the 16 July 2008 THEMIS Observations Compared to the Vlasiator Run

	IMF (nT)	Cone angle (deg)	Density (cm ⁻³)	Velocity (km/s)
Vlasiator	[-4.9, 0.4, 0]	5	3.3	600
THEMIS	[4.8, -1.6, -0.2,]	19	1.8	666

with a down-scaled geomagnetic dipole. Despite the consequent uncertainties in the scale sizes of the system and even though the ion distribution functions have suffered from the limited number of particles used in the simulation, this approach has been able to reproduce the wave characteristics. *Blanco-Cano et al.* [2009] investigated the ULF waves under radial IMF conditions but did not identify a mechanism for the oblique propagation angle. Recently, a new global approach complementary to the hybrid-PIC based on the hybrid-Vlasov approach has been developed [*Palmroth et al.*, 2013; *von Alfthan et al.*, 2014]. This approach is computationally more demanding than the hybrid-PIC, and it does not track the origin of particles inherently. However, the hybrid-Vlasov method produces an improved representation of the ion distribution function [*Pokhotelov et al.*, 2013; *Kempf et al.*, 2015] without the numerical noise, and it is able to model the system without scaling the geomagnetic dipole strength, leading to correct scale sizes of the system.

This article investigates the foreshock ULF waves under the special condition of nearly radial IMF, using the Vlasiator simulation in a two-dimensional setup. The target is first to investigate the ULF wave characteristics and to validate the simulation results by comparing to earlier literature and experimental data recorded by Time History of Events and Macroscale Interactions during Substorms (THEMIS) spacecraft [*Angelopoulos*, 2008]. Second, the almost radial IMF introduces an opportunity to investigate the oblique propagation of the waves. The article is structured as follows: First, we briefly describe the Vlasiator simulation and the run setup for the radial IMF case. We then investigate the ULF wave characteristics within the foreshock and compare to earlier literature. In section 4, we compare the characteristics to THEMIS observations. Finally, we discuss the problem of oblique propagation and present an initial idea for the oblique propagation mechanism under radial IMF, informed by the Vlasiator simulation results.

2. Model Description

Vlasiator is a newly developed global hybrid-Vlasov model, where protons are described by the full distribution function $f(\mathbf{r}, \mathbf{v}, t)$ in the phase space, and electrons are treated as a charge-neutralizing fluid [*von Alfthan et al.*, 2014]. This approach neglects electron kinetic effects but includes the ion kinetic effects without the numerical noise present in hybrid-PIC methods, in which the distribution function noise is typically controlled by increasing the number of launched particles. The time evolution of $f(\mathbf{r}, \mathbf{v}, t)$ is given by the Vlasov equation, propagated by a fifth-order accurate semi-Lagrangian approach [*Zerroukat and Allen*, 2012; *White and Adcroft*, 2008]. The electromagnetic fields are solved using Maxwell's equations neglecting the displacement current in the Ampère-Maxwell law. Maxwell's equations are supplemented by Ohm's law, including the Hall term neglected in previous Vlasiator versions [*Palmroth et al.*, 2013; *von Alfthan et al.*, 2014; *Kempf et al.*, 2015]. The closure scheme, the numerical approach, and the parallelization description can be found in *von Alfthan et al.* [2014], while newer additions to the code include the semi-Lagrangian solver replacing the older Finite Volume Method and the Hall term in Ohm's law.

Vlasiator was used to simulate an event with almost radial IMF conditions. The time-stationary solar wind conditions are given in Table 1. Due to computational resource limits, in this run the simulation box is 5-D, where the ordinary space is solved in the ecliptic XY plane of the Geocentric Solar Ecliptic (GSE) coordinate system, while each ordinary space cell includes a separate velocity space self-consistently coupled to the ordinary space. The box size in ordinary space in this run is from $-7 R_E$ to $60 R_E$ in X , and ± 30 in Y , with a resolution of 227 km, while the ion inertial length in this run is 125.4 km (see Table 1). The velocity space resolution is 30 km/s. The solar wind conditions are introduced at the sunward wall of the simulation box, while at other boundaries copy conditions are employed, i.e., the full distribution function is copied from the nearest spatial cell that is inside the simulation domain. Periodic boundary conditions are applied in the Z direction of the ordinary space. The inner edge of the magnetospheric domain is set at a circle with a radius of $5 R_E$, from where the dipole field is mapped to the ionosphere, which currently is a perfect conductor. Vlasiator uses the actual unscaled geomagnetic dipole strength as a boundary condition.

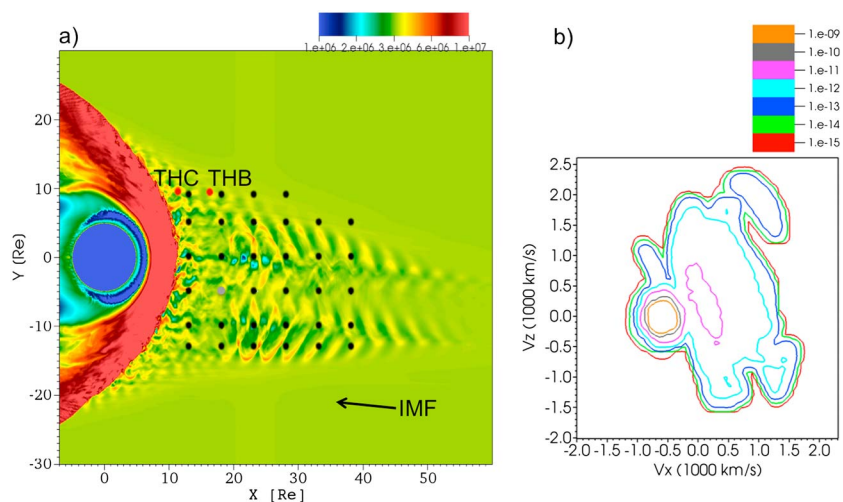


Figure 1. (a) Color coding shows Vlasiator's modeling of logarithm of plasma density within the Earth's foreshock at time 500 s from the start of the simulation in SI units, m^{-3} . The black dots indicate the positions of virtual spacecraft, where data for the analysis are taken from. The grey dot indicates the position of the virtual spacecraft for which data are given in Figure 2. The two red dots indicate the positions of THEMIS C (closer to shock surface) and THEMIS B (further from the shock surface), for reference. (b) Example of the distribution function at position $[X, Y] = [18, -5] R_E$ (colored with a grey dot) as a cut in the velocity XZ plane, again in SI units, $s^3 m^{-6}$.

3. Modeling Results

Figure 1a shows an overview of Vlasiator modeling of plasma density in the ecliptic plane under quasi-radial IMF conditions with 5° cone angle. The color coding is taken from one time instant in the run, representing 500 s from the beginning of the run, by which time the foreshock has already developed. Magnetosheath is shown as red and is bound on its inner and outer edges by the magnetopause and bow shock, respectively. The black dots indicate the positions of virtual spacecraft for which time series data are taken from the simulation for later analysis, while the grey dot is the position of the virtual spacecraft for which data are given in Figure 2. The red dots refer to section 4 and are discussed there. Figure 1b shows an example of the distribution function at position $[X, Y] = [18, -5] R_E$, as a cut of the velocity XZ plane.

Figure 1a indicates that the foreshock wave field is visible approximately at $10 R_E$ to $50 R_E$ in the X and about $\pm 15 R_E$ in Y , while at later time instants the wave field extends to the edge of the simulation domain in $+X$. The plasma density shows clear oblique wavefronts bent in many directions with respect to the ambient IMF. The wavefronts appear generally structured around and along two "backbones" or "spines" extending along the X axis, at approximately $Y = -12$ and $2 R_E$. Further, there is a clear difference in the oblique angle between the edges of the foreshock and the central foreshock. The solar wind advects the wavefronts toward the bow shock surface (as shown in Movie S1 given as supporting information to this paper). Around $[X, Y] = [20, 0] R_E$, the wavefronts show isolated areas of decreased density in comparison to the surrounding plasma, which appear to be consistent with the known properties of foreshock cavitons [Blanco-Cano et al., 2011]. Figure 1b presents two plasma populations, the core solar wind flowing with the solar wind velocity toward the Earth, and the population reflected at the bow shock, streaming along the positive X with approximately the speed of 500 km/s. For a more detailed discussion of the distribution function structure, see Kempf et al. [2015].

Figure 2 shows temporal data from the virtual spacecraft positioned at $[X, Y] = [18, -5] R_E$ (cf. Figure 1). Figures 2a–2e show density, magnetic field intensity $|B|$, and x , y , and z components of the magnetic field, respectively, as a function of time in the simulation. The density fluctuations are about 10–15% of the ambient solar wind. The fluctuations before about $t = 520$ s are more evenly structured, while after $t = 520$ s the virtual spacecraft is collocated with a region where the wave frequency and density amplitude increases. This region is the outskirts of the caviton-like structure visible in Figure 1. The waves are compressive, as they also have a magnetic depression of about 10–20% of the ambient magnetic field intensity (Figures 2b–2e), in line with, e.g., Le and Russell [1994] and Eastwood et al. [2002]. The caviton-like structure exhibits smaller magnetic field fluctuations, consistent with typical features related to cavitons [Blanco-Cano et al., 2011].

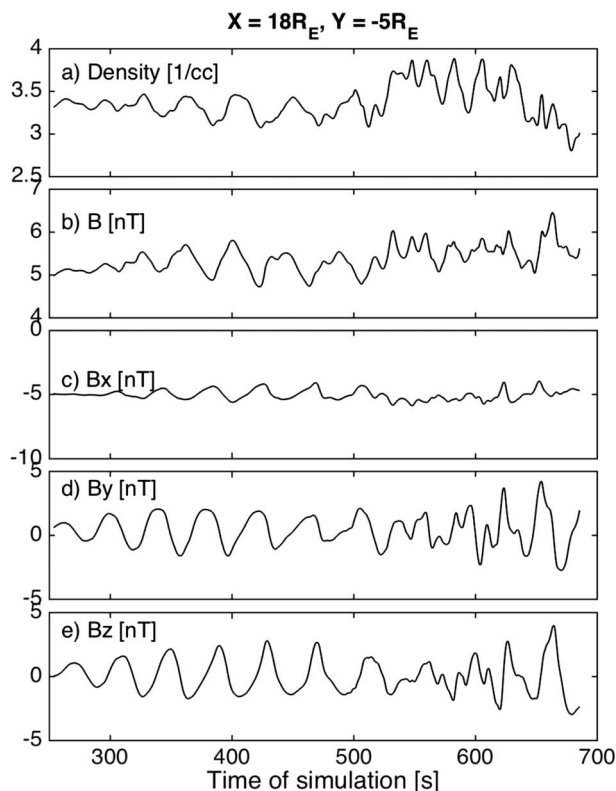


Figure 2. Time series of the virtual spacecraft in Figure 1 from the position $[X, Y] = [18, -5] R_E$. (a) Plasma density, (b) magnetic field intensity, (c–e) x, y, and z components of the magnetic field, respectively, against time in simulation.

The Fourier transform of the magnetic field fluctuations (not shown) reveals clear peaks in the power spectral density at frequencies of 0.023 Hz, 0.025 Hz, 0.025 Hz, and 0.023 Hz as deduced from a Fourier transform using B_x , B_y , B_z , and B , respectively, corresponding to wave periods of 40 s and 43.5 s. For a cone angle of 5° , an estimation based on empirical observations should be about 0.037 Hz, corresponding to a period of 27 s [Takahashi *et al.*, 1984].

Figure 3a shows a histogram of the wave periods, evaluated using the virtual spacecraft time series of the magnetic field z component. Even though there are 34 virtual spacecraft from which temporal data are analyzed, the Fourier spectrogram may exhibit more peaks at a single position, and hence there are more than 34 entries in Figure 3a (only peaks above 40% of the maximum power spectral density are considered here). Figure 3a shows that most of the foreshock waves have a period of 30–40 s, while there are also longer and shorter period waves present. This is consistent with Eastwood *et al.* [2005a]. Other components of the magnetic field and the magnetic field intensity yield similar results for the period histogram.

Figure 3b presents a histogram of the angle of propagation of the foreshock wavefronts. The angle is calculated using the virtual spacecraft magnetic field time series as input to a minimum variance analysis, where the minimum variance direction gives an estimate of the wave vector \mathbf{k} [e.g., Hoppe *et al.*, 1981]. The dot product of \mathbf{k} with the ambient IMF direction gives θ_{kB} , which is the angle at which the wavefront propagates with respect to the magnetic field. Figure 3b indicates that θ_{kB} varies mostly between 0° and 20° , peaks below 10° , while larger angles are not absent. Again, this is in good agreement with Eastwood *et al.* [2005b], reporting that even with cone angles reaching radial IMF conditions the propagation angle is approximately between 5° and 20° (see Figure 5 of Eastwood *et al.* [2005b]).

Figure 4 presents the foreshock wave field as a color plot of the B_z component representing an Alfvénic disturbance. The figure (like Figure 1) is a snapshot at 500 s from the beginning of the simulation. Overlaid with B_z are contours of B_y that illustrate the waves. Black vectors are the x and y components of the minimum variance direction representing the wavefront orientation. The minimum variance direction is calculated from the

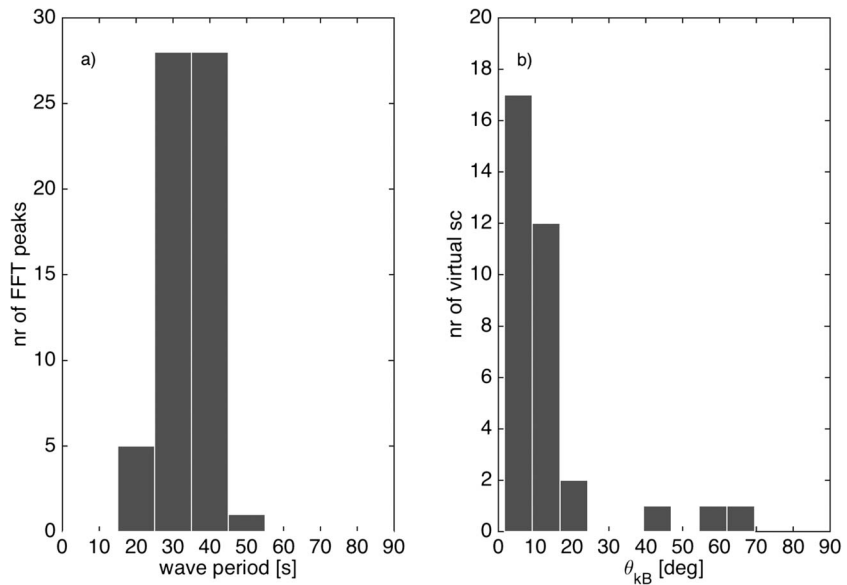


Figure 3. (a) Histogram of the wave periods from the virtual spacecraft positions in Figure 1, evaluated from the Fourier transform of the magnetic field z component. (b) Histogram of the wave propagation directions with respect of the ambient IMF (θ_{kB}), evaluated using the virtual spacecraft time series in the minimum variance analysis.

temporal magnetic field data of the virtual spacecraft using all simulation data during which the virtual spacecraft is within the foreshock proper (see Figure 1). The colored straight lines through the duskside, central, and dawnside of the foreshock refer to Figure 6.

Let us first scrutinize the wavefronts using the color plot and the contours. Generally, the foreshock waves have oblique orientations tilted toward both positive and negative Y axis. The waves being born at the largest distances from the bow shock are roughly perpendicular to the magnetic field, before they are advected toward the bow shock surface. Typically, the wavefronts are bent toward the positive (negative) Y axis near

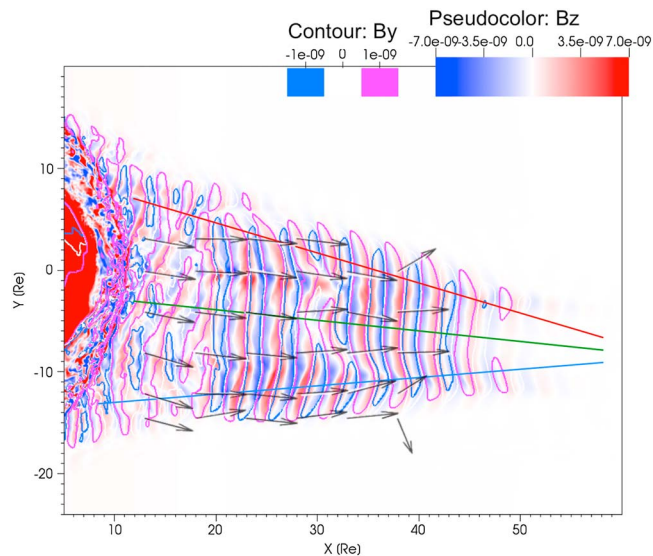


Figure 4. Color coding shows the simulation B_z component representing an Alfvénic disturbance, while the contours are taken from B_y illustrating the wavefronts. The arrows are the x and y components of the minimum variance directions calculated from the virtual spacecraft magnetic field temporal data. The red, green, and blue lines in the dusk, central, and dawn edge of the foreshock, respectively, are used to illustrate where data are taken for the wavelength analysis discussed in Figure 6.

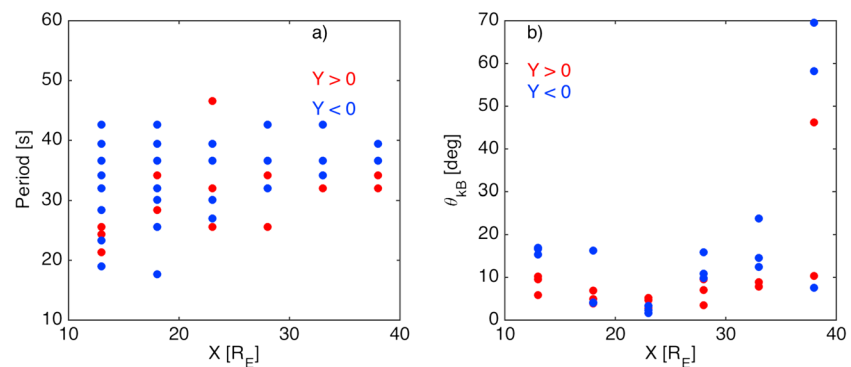


Figure 5. (a) Wave period against virtual spacecraft location on X axis, with those periods based on time series of virtual spacecraft located in the duskside (dawnside) foreshock as red (blue). (b) Wave propagation direction with respect to the IMF direction against the virtual spacecraft location on X axis with similar color coding as in Figure 5a.

the foreshock edges at positive (negative) Y . Near the bow shock surface closer than approximately $20 R_E$, the wavefront orientations become more disorganized.

Figure 4 illustrates that the minimum variance direction is generally a good indication of the wavefront orientation in the foreshock. In 25 cases out of 34, the intermediate to minimum eigenvalue ratio of the minimum variance analysis is larger than 8, while in two cases it is between 1.8 and 2, indicating that generally the minimum variance analysis can be trusted [Eastwood *et al.*, 2002]. Furthermore, near the bow shock surface, the waves are not as coherently oriented as further upstream; and hence, the minimum variance direction also slightly deviates from the wavefront normal direction at the corresponding virtual spacecraft positions.

Figure 5 illustrates the wave period and propagation angle characteristics more quantitatively as a function of location in the foreshock. Figure 5a shows the wave period as a function of distance along the X axis, as determined by Fourier analysis of the virtual spacecraft B_z measurements. The wave periods from time series that have been observed in the duskside (dawnside) of the foreshock have been colored red (blue), respectively. The wave periods have a larger variation near the bow shock most probably due to more turbulent conditions there, while further upstream in the foreshock the waves are more consistently of the same period (30–40 s). The waves in the duskside foreshock have shorter periods than waves in the dawn foreshock.

Figure 5b shows the wave propagation angle with respect to the IMF direction as measured from the minimum variance analysis. Consistent with the visual analysis in Figure 4, there is a clear break point in the propagation angle at $23 R_E$. Upstream of this distance, the wave propagation angles vary considerably. At $23 R_E$, the wave propagation angle is the smallest throughout the foreshock, while downstream of this distance the propagation angle spreads again, although this is not as pronounced as in the upstream area. The dawnside propagation angles tend to be slightly more oblique throughout the foreshock compared to the duskside propagation angles. Based on Figures 5a and 5b, we conclude that the waves in the dusk foreshock appear shorter in period and their propagation angle is more aligned with the IMF, while the dawn foreshock waves have a larger period and a larger propagation angle with respect to the IMF.

Figures 6a–6c shows the B_z component evaluated at the duskside, central, and dawnside of the foreshock, at lines through the ordinary space illustrated with red, green, and blue colors, respectively, in Figure 4. Figures 6a–6c indicate fully developed wave activity throughout the foreshock, with more evenly structured waves further upstream, and more deformed waves near the bow shock surface. There are high-amplitude perturbations with apparently shorter wavelength which appear near the bow shock surface. Especially close to the dawn edge of the foreshock, the wave amplitudes are relatively smaller near the bow shock surface and far upstream, while larger amplitudes are observed at distances of about $30 R_E$ from the shock surface. In the central foreshock, the wave amplitudes are pronounced throughout, with the exception of the far upstream area. The waves appear to grow more easily at the edges of the foreshock, while the waves in the central foreshock appear to grow at slightly smaller distances; this can also be seen in the color coding in Figure 4.

To evaluate the wavelength in Figure 6d, we plot the distance between the wave peak amplitudes along each line, using the same color coding, i.e., the red dots show the distance between the peak amplitudes on the red curve (Figure 6a), which is a cut through the duskside of the foreshock (see Figure 4). Note that the

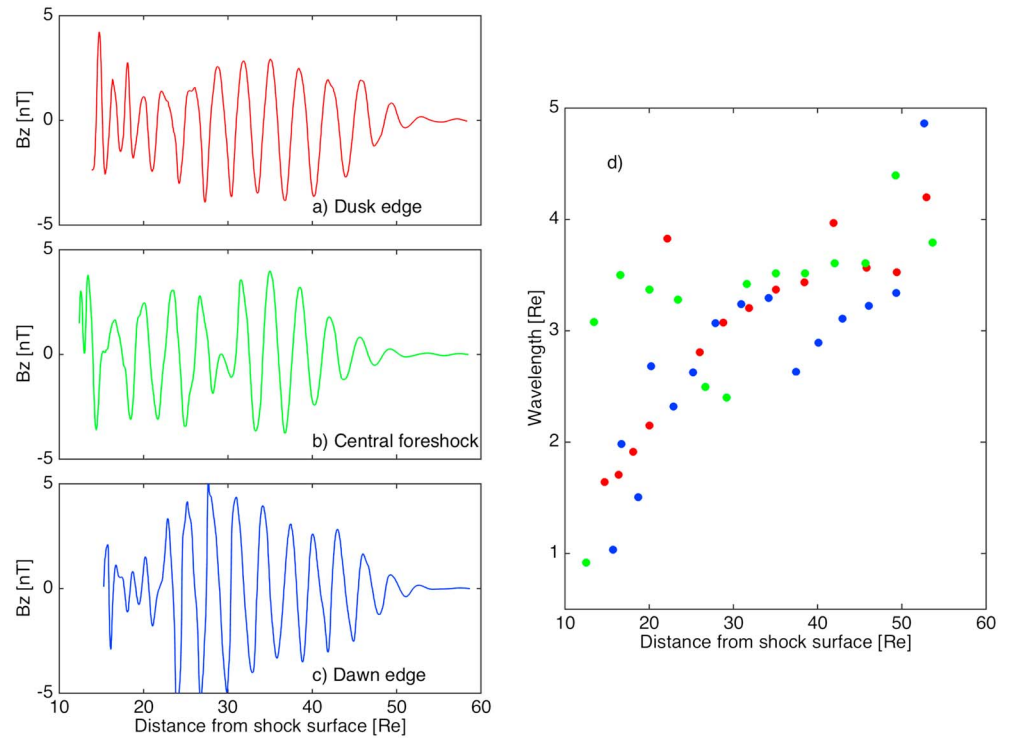


Figure 6. (a–c) B_z component taken at the duskside, central, and dawnside of the foreshock, respectively, along the distance of red, green, and blue lines illustrated in Figure 4. Distance is evaluated as $\sqrt{X^2 + Y^2 + Z^2}$ of the line coordinates. The data are taken at lines which are cuts through space at the time instant 500 s, when the foreshock is fully developed. (d) The wavelength of the B_z components in Figures 6a–6c, using the same color coding. The wavelength is evaluated as a distance between peak values and plotted as a function of distance on the line.

wavelength is measured along the spatial cut that is not exactly parallel to the individual wave \mathbf{k} . Figure 6 illustrates that the wavelengths vary approximately between 1 to 4 R_E , in accordance with *Le and Russell* [1994]. The wavelengths decrease toward the shock surface. In particular, we note that the wavelengths increase with increasing distance from the shock at the edges of the foreshock, while in the central foreshock the effect is not as clear.

In the perpendicular direction, the wave sizes depend on the distance from the bow shock. Figure 4 indicates that near the bow shock surface the lengths of the wavefronts are about 5 R_E and upward in the perpendicular direction. Further upstream, some wave fronts can extend across the entire foreshock; and hence, the perpendicular scale, e.g., at $X = 25 R_E$, can be over 20 R_E . Furthest upstream, the wave perpendicular scales are again closer to 5 R_E . *Archer et al.* [2005] report wave sizes from 8 to 18 R_E perpendicular to \mathbf{k} , in agreement with the results here.

Finally, we investigate the polarization of the foreshock wave field. Figure 7 shows the wave field polarization using data from the virtual spacecraft positioned at $[18, -5] R_E$ (see Figure 1), for the time period 255.5–474.5 s (see Figure 2), i.e., neglecting the waves associated with the region of caviton-like structures visible in Figure 1. For evaluating the polarization, we define $\Delta\mathbf{B}$ by removing the background magnetic field from the virtual spacecraft measurement. Then, we define a projection of the magnetic field in the XY plane as a dot product of the $\Delta\mathbf{B}$ with a unit vector in the XY plane, defined as the cross product of the Z axis and the wave normal from the minimum variance analysis. Figure 7 shows the wave magnetic field in the XY plane against the wave magnetic field in the Z direction such that the direction toward the viewer is the wave \mathbf{k} in the direction of the IMF, while the circle indicates the start of the time series. The polarization is elliptical and left handed in the virtual spacecraft frame with respect to the magnetic field direction. However, polarization is defined in the plasma rest frame, and if the wave vector and the advection velocity are antiparallel, as is the case with the foreshock waves, the handedness of the waves flips, making the intrinsic polarization of the waves in Figure 7 elliptical and right handed. This is again in accordance with several previous papers [e.g., *Hoppe et al.*, 1981; *Le and Russell*, 1994; *Eastwood et al.*, 2002, 2005a].

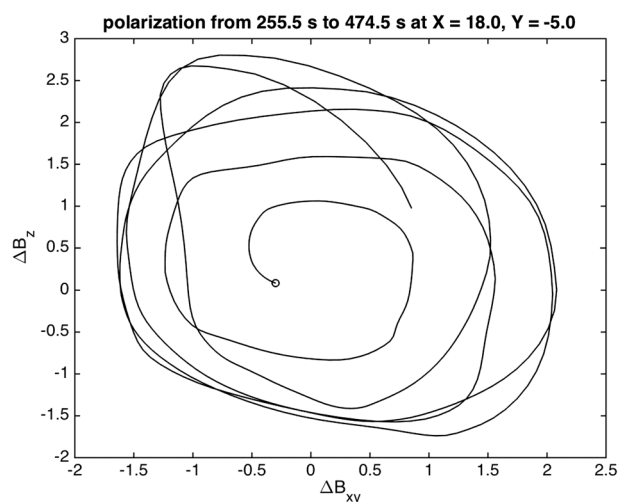


Figure 7. Polarization of the foreshock wave field at virtual spacecraft position [18, -5] R_E during 255.5–474.5 s (see Figure 2), with the IMF direction out of the plane toward the viewer. The open dot marks the start of the data set, indicating that the wave is left handed in the virtual spacecraft frame of reference.

4. Observations

Next, we wish to investigate, using spacecraft observations, how the Vlasiator modeling results correspond to actual foreshock wave properties. We searched the THEMIS 2008 dayside season for periods with similar solar wind conditions whereby multipoint spacecraft observations in the foreshock were available. This resulted in one suitable event on 16 July 2008, when two of the THEMIS spacecraft (THEMIS B and THEMIS C) encountered the foreshock region during which time the IMF vector $\mathbf{B} = [4.8, -1.6, -0.2]$ nT, corresponding to an IMF cone angle of 19° . This IMF direction is almost antiparallel to the Vlasiator case. Table 1 shows a comparison between the solar wind and IMF parameters for the Vlasiator run and the THEMIS event. We used lagged L1 data (which was validated by comparison with THEMIS) from the OMNI database compiled at National Space Science Data Center (<http://spdf.gsfc.nasa.gov/>). Figure 1a shows the THEMIS positions in the Vlasiator modeling of the foreshock using the geocentric interplanetary medium (GIPM) coordinate system [Bieber and Stone, 1979], which rotates about the Sun–Earth line such that the IMF is entirely in the second and fourth quadrants of XY plane. This makes the GIPM $Z = 0$ direction comparable to the simulation. In the THEMIS interval the z component of the IMF is small; and hence, there is little difference between GSE and GIPM.

Figure 8 shows THEMIS B and THEMIS C Fluxgate Magnetometer [Auster et al., 2008] and combined electrostatic analyzer and solid state telescope [McFadden et al., 2008] data in Figures 8a–8d and 8e–8h, respectively, on 16 July 2008. In THEMIS B, there is a noticeable slope in B_z and B_y , and there are no suprathermal ions or upstream waves before about 23:04 UT. At 23:04 UT, the ions with energies up to 4 or 5 keV are reflected field-aligned ion beams (distributions not shown). This indicates that the spacecraft was outside the foreshock in the beginning of the plotted period. After this, a correlated compression in magnetic field and density follows as higher-energy ions are observed, followed by ULF upstream waves. The transient signature is likely due to the motion of the foreshock compressional boundary [e.g., Sibeck et al., 2008] in response to slight IMF changes. Therefore, consistent with Figure 1a, THEMIS spacecraft are near the foreshock boundary during the event.

Throughout the plotted period, both THEMIS B and THEMIS C show fluctuations in the magnetic field B_z and B_y components, while the fluctuations in B_x are smaller. The density fluctuations in concert with the magnetic field are indicative of compressive waves, and as the fluctuations are accompanied by suprathermal ions, we conclude that the spacecraft are in the ULF foreshock and observe upstream ULF waves [Le and Russell, 1994]. At THEMIS C, which is close to the bow shock surface, the fluctuations are larger both in the magnetic field and in density, signifying wave growth toward the bow shock.

Figure 9 shows the Vlasiator data at THEMIS B and THEMIS C as defined in Figure 1. The simulation time is the same as physical time. Figures 9a and 9c are the magnetic field components and intensity, while Figures 9b and 9d are the plasma density. The color coding and the axis limitations are the same as in Figure 8 to facilitate

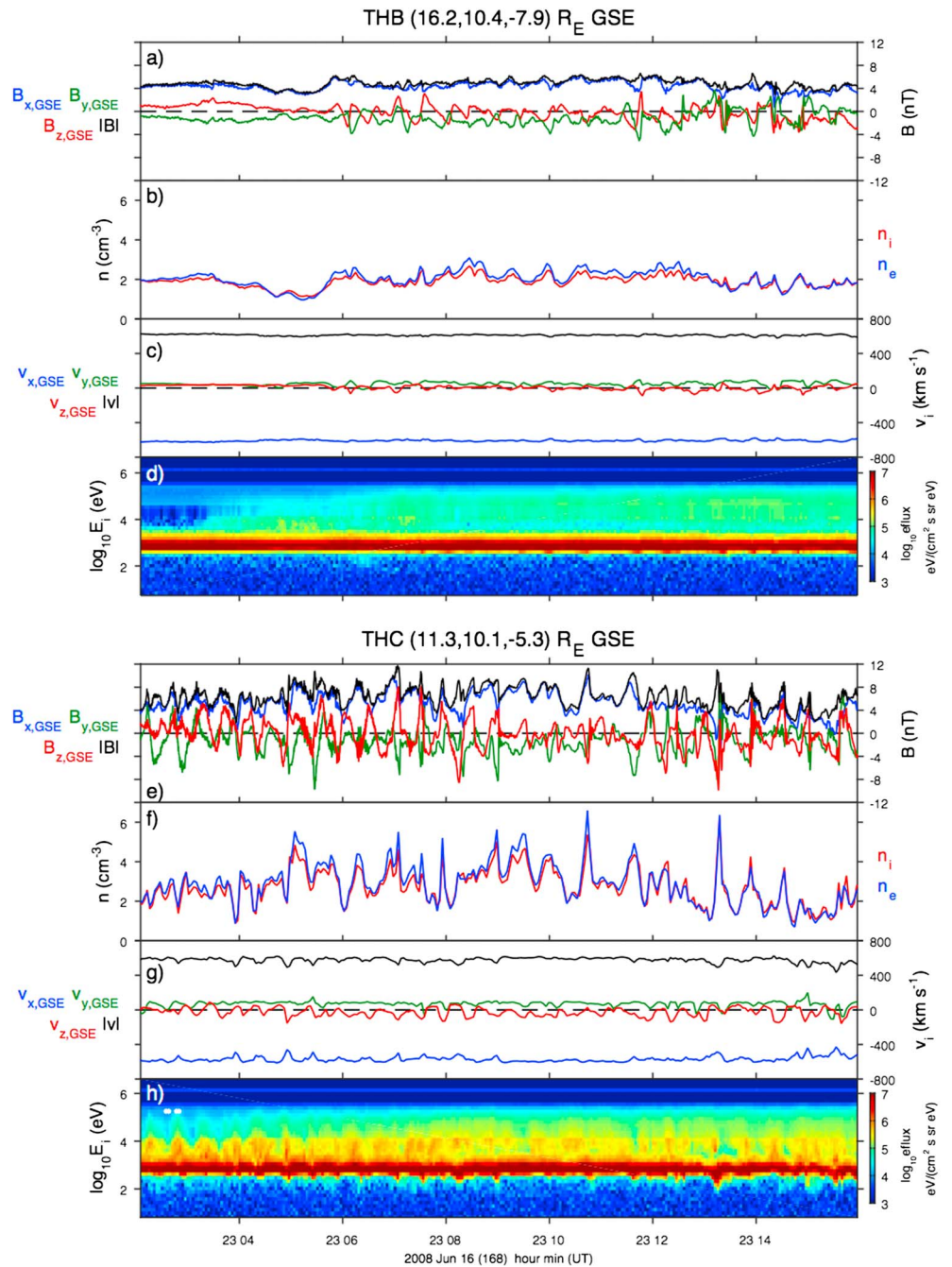


Figure 8. THEMIS B observations for (a) magnetic field components B_x , B_y , B_z in blue, green, and red, respectively, and magnetic field intensity (black), (b) density (as measured both from ions and electrons in red and blue, respectively), (c) velocity components v_x , v_y , and v_z in blue, green, and red, respectively, and speed (black), and (d) ion energy spectrogram with the color indicating differential energy flux. (e–h) The observations from THEMIS C in the same format.

comparison to spacecraft observations. At THEMIS B positioned upstream of THEMIS C, the fluctuations are similar in magnitude as in observations, while at THEMIS C position the Vlasiator modeling does not show a similar compression. Looking at Figure 6a, the duskside cut through the foreshock shows that the wave amplitudes are large near the bow shock, then decrease somewhat, but are largest around 30–40 R_E distance. Note that as THEMIS B is further upstream compared to THEMIS C, the Vlasiator foreshock starts to develop later in the simulation, while at the THEMIS C position the ULF fluctuations start sooner.

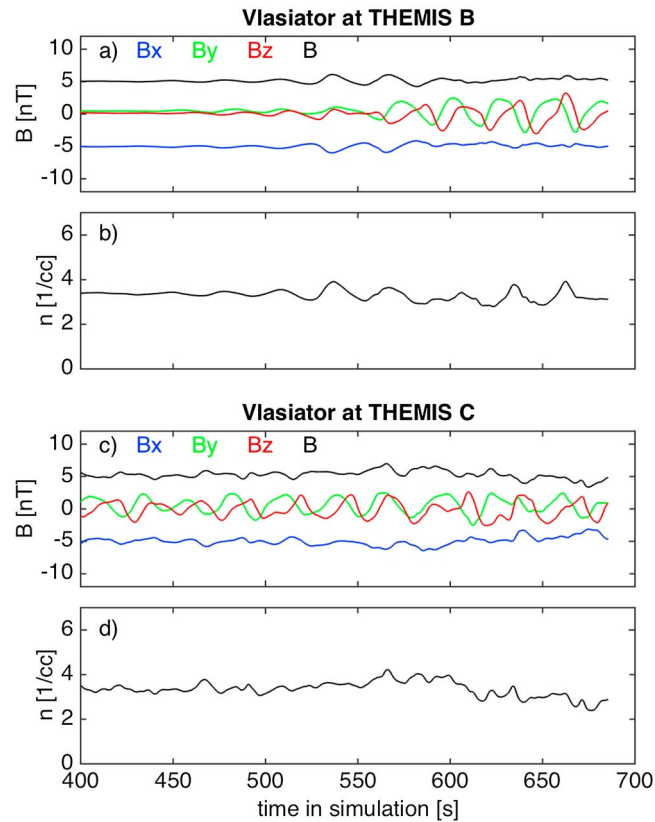


Figure 9. (a and b) Vlasiator results at THEMIS B and (c and d) THEMIS C spacecraft position. Figures fig:VTHa and fig:VTHc are the magnetic field components B_x , B_y , and B_z in blue, green, and red, respectively, and magnetic field intensity (black). Figures fig:VTHb and fig:VTHd are the density.

Table 2 gives a summary of the detailed comparison between THEMIS and Vlasiator. According to the *Takahashi et al.* [1984] formula, the frequency of upstream ULF waves in the subsolar foreshock should be 0.035 Hz during the THEMIS event, corresponding to a period of 29 s. This is in good agreement with the THEMIS data. For the simulated case, the *Takahashi et al.* [1984] formula predicts a period of 27 s using the run cone angle and IMF strength, again corresponding well with the simulation values. To compute θ_{kB} , the observations were subdivided into 2 min intervals (50% overlap) and minimum variance analysis was applied to each interval having 3 s smoothed time series. The smoothing was done to remove higher-frequency whistler waves known to exist in the foreshock alongside the 30 s waves [*Hoppe et al.*, 1981], so that the θ_{kB} corresponds to the 30 s waves. In the used version of Vlasiator such higher-frequency waves are not present; and hence, the simulation data did not have to be smoothed. The average θ_{kB} is given as the angle between the average (over the components) minimum variance direction and the IMF, whereas the error indicates the directional spread around this average direction. The approach is similar to that used by *Eastwood et al.* [2004, 2005b]. While the average θ_{kB} are slightly larger in Vlasiator than in the observations, there is a systematic decrease in

Table 2. Wave Characteristics in THEMIS and Vlasiator, Using the GIPM Coordinate System^a

	THEMIS B	Vlasiator	THEMIS C	Vlasiator
$[X, Y, Z]_{\text{GIPM}}$	[16.2, 9.3, -9.1]	[16.2, 9.3, 0]	[11.3, 9.4, -6.5]	[11.3, 9.4, 0]
Period (B_x)	39 s	29 s	32 s	31 s
Period (B_y)	33 s	26 s	30 s	28 s
Period (B_z)	33 s	26 s	28 s	28 s
Period (B)	39 s	32 s	39 s	31 s
θ_{kB}	$20^\circ \pm 36^\circ$	$24^\circ \pm 18^\circ$	$10^\circ \pm 39^\circ$	$15^\circ \pm 14^\circ$

^aTHEMIS data are based on analysis during the period of ULF waves.

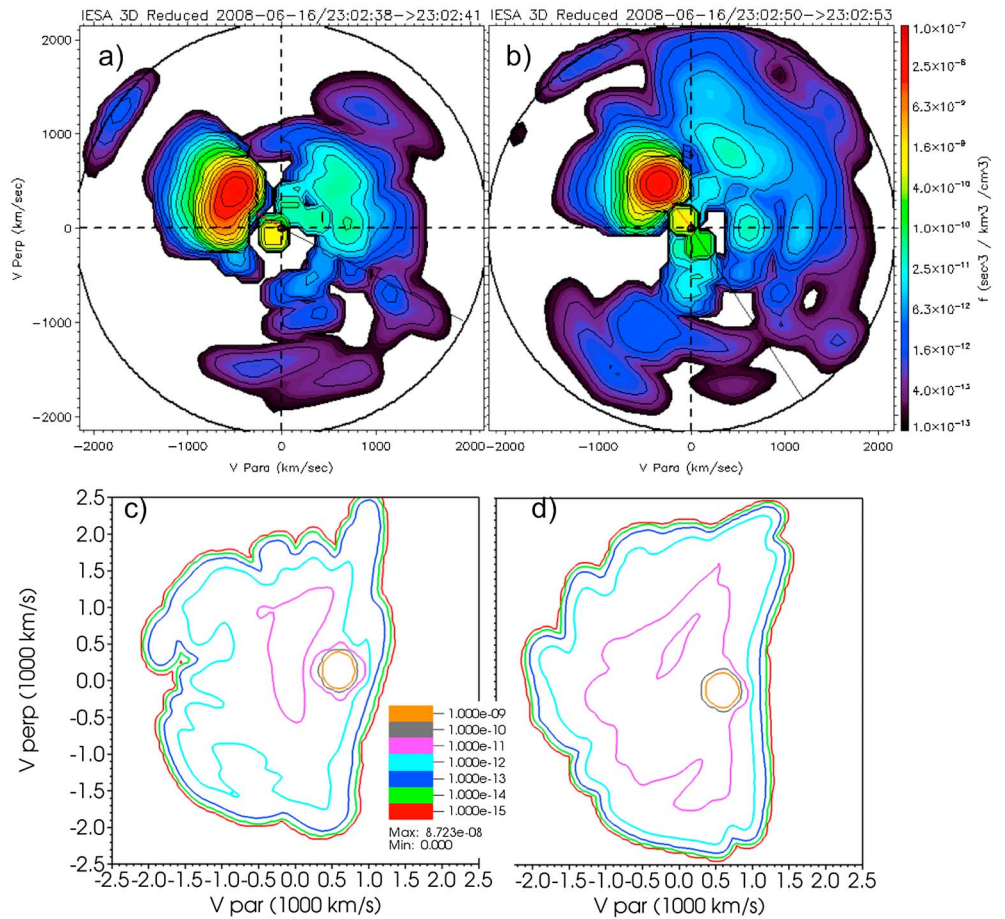


Figure 10. (a and b) THEMIS C, respectively, outside and during the enhancements in the suprathermal ion energy flux visible in Figure 8h. (c and d) The Vlasiator distributions taken at the THC position in the GIPM frame at time $t = 500$ s and $t = 685$ s, respectively. Note that the IMF in the simulation is antiparallel to the THEMIS data; hence, the beams are also antiparallel in this projection, making the distribution function mirrored.

θ_{kB} further downstream. Furthermore, in the plane defined by the magnetic field and solar wind velocity, the \mathbf{k} deflection systematically points toward the foreshock edge at THB to being more field aligned at THC. This is common to both the observations and Vlasiator. The large spread in the observations is in part due to some poor eigenvalue ratios leading to a larger error in minimum variance analysis.

Figure 10 shows examples of the distribution function observed by THEMIS C observations of the ion velocity distribution function (Figures 10a and 10b), accompanied by a Vlasiator distribution function (Figures 10c and 10d) at THEMIS C location. All data are given in the coordinates parallel and perpendicular to the magnetic field. The times at which the distributions are taken are marked in Figure 8 by white horizontal bars in Figure 8h. Figures 10a and 10b, respectively, are taken outside and during the enhancements in the suprathermal ion energy flux visible in Figure 8h, i.e., times when the color scale is more orange at energies 3000–10,000 eV. The enhancements have the same periodicity as the ULF waves. The Vlasiator distributions (Figures 10c and 10d) are taken at the THC position in the GIPM frame at time $t = 500$ s and $t = 685$ s, respectively. The THEMIS C distribution functions show that the suprathermal distributions are more field aligned or intermediate outside the enhancements (Figure 10a) and hotter and more diffuse like during the enhancements (Figure 10b). Therefore, the upstream ULF waves may modulate the beam and the shock thereby changing the ion distributions as reported by Mazelle *et al.* [2003] and Meziane *et al.* [2001, 2004]. Vlasiator distributions taken from the THC position and displayed in Figure 10 first show a relatively hot field-aligned/intermediate beam (Figure 10c), while later the distribution is more diffuse (Figure 10d), in accordance with THEMIS C observations. This indicates a temporal dependency within the same location, while the spatial dependency of the Vlasiator distribution function is addressed more in Kempf *et al.* [2015].

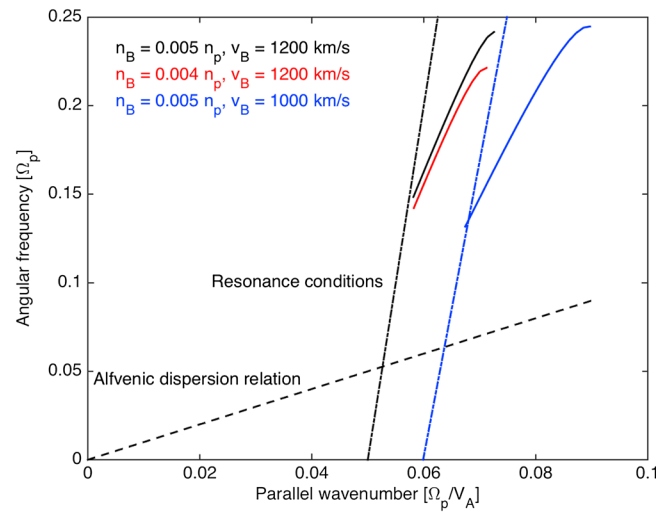


Figure 11. Dispersion relation of parallel-propagating right-hand polarized unstable waves in a beam plasma, with varying beam density and velocity, color coded as indicated in the legend. Displayed also are the Alfvénic dispersion relation and the resonance conditions for the two beam velocities.

concerns the entire foreshock. The comparison with THEMIS data shows that Vlasiator results at the spacecraft locations are in quantitative agreement with the observations. The THEMIS data show that the distribution functions are modulated with the waves, which has been attributed to wave modulation of the shock properties. This is also seen when scrutinizing the Vlasiator distribution functions, in line with earlier observations [Meziane et al. 2001, 2004]. We therefore conclude that the Vlasiator ULF foreshock reproduces the ULF foreshock characteristics such that the modeling results can be used to make physical conclusions based on the simulation.

Even though we present modeling results during stationary solar wind conditions, there is considerable variability in the wave characteristics throughout the foreshock. The wave characteristics are in agreement with previous statistics [Eastwood et al., 2005a, 2005b] that are measured during a variety of solar wind conditions, indicating that the foreshock physics is not only driven by external solar wind conditions but also influenced by the intrinsic properties of the foreshock. The wave characteristics show generally more variability near the bow shock and are more coherent further upstream. This is probably due to the more turbulent conditions near the bow shock, where the waves evolve nonlinearly as they advect, and where the shock rippling also affects the wave field characteristics. There is also a considerable variability in the Y direction through the foreshock, which we discuss shortly.

To investigate the oblique propagation, we show in Figure 11 first (as a dashed black line) the Alfvénic dispersion relation of low-frequency waves approximated by $\omega = k_{\parallel} v_A$, and second as solid lines the dispersion relation of the right-handed elliptically polarized waves for a plasma consisting of a solar wind core and a reflected ion beam population. The latter dispersion relation has been obtained using the WHAMP code calculating the dispersion relation of Waves in Homogeneous Anisotropic Magnetized Plasma [e.g., Kempf et al., 2013] with parameters representative of the Vlasiator foreshock in the radial run presented in this paper. Only the dispersion relation where the growth rate is larger than 0.02 is shown. To illustrate the dependence of the dispersion relation on the beam properties, we vary the beam density and beam velocity. The black curve represents a plasma with beam density n_B of 0.5% of the solar wind density, and beam velocity v_B of 1200 km/s. The red curve is with the same beam velocity with a smaller beam density, while the blue curve is with the same beam density with a smaller beam velocity relative to the black curve. As can be seen in Figure 11, the dispersion relation differs qualitatively from the standard Alfvénic dispersion relation. To the lowest order, the dispersion relation is of the form

$$\omega = -a(n_B)\Omega_p + b(n_B)v_B k_{\parallel} \quad (1)$$

where a and b are positive dimensionless constants depending on the beam density n_B , Ω_p is the proton cyclotron frequency, v_B is the beam speed and k_{\parallel} is the wave number parallel to the magnetic field.

5. Discussion

In this paper we have presented the first detailed modeling results of the ULF foreshock wave field under radial IMF conditions using the new Vlasiator simulation and compared them to a representative case from THEMIS data records as well as to long known properties of ULF waves from previous studies. The ULF wave periods, propagation angles, polarization, and wavelengths both in the parallel and perpendicular direction are in accordance with previous literature [Le and Russell, 1994; Eastwood et al., 2005a, 2005b; Archer et al., 2005]. Note that a typical spacecraft apogee is about $20 R_E$ indicating that the main observational statistical results concern wave properties relatively close to the bow shock, while our analysis concerns the entire foreshock.

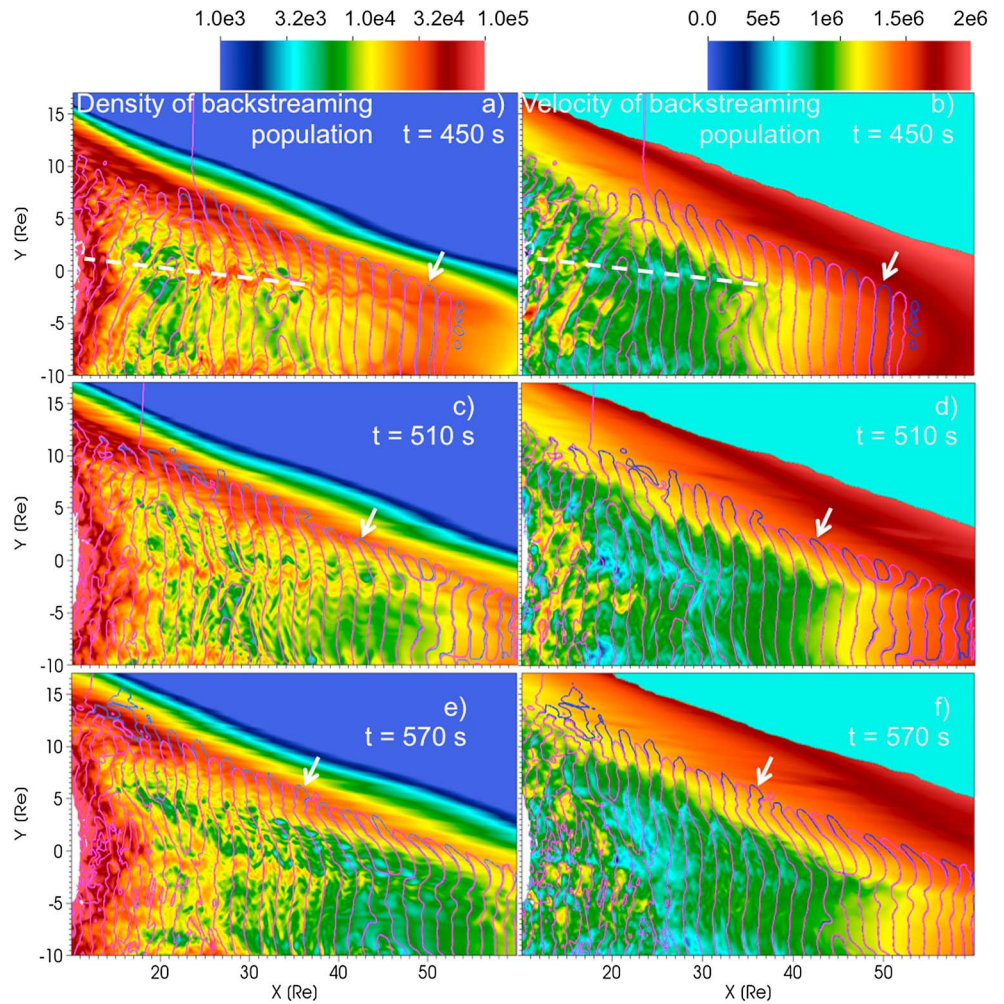


Figure 12. (a, c, e) Density and (b, d, f) velocity relative to the solar wind core population of the back streaming population, for three time instants, 450 s (Figures 12a and 12b), 510 s (Figures 12c and 12d), and 570 s (Figures 12e and 12f). Contour lines show B_z at values -0.01 nT (blue) and 0.01 nT (red) illustrating wavefronts. The white arrows identify an individual wavefront, being born perpendicular to the magnetic field direction, and later becoming oblique (see text for details).

As the dispersion relation shows, the wave number k depends on the beam speed and the beam density. Therefore, we present the density and the velocity of the back streaming population relative to the solar wind core population in Figure 12 for three different times. The white arrows identify an individual wavefront, illustrated with B_z contours. To separate the solar wind core population from the back streaming one, all velocity space within a sphere of radius ~ 690 km/s centered on the upstream solar wind velocity is considered to be the solar wind population, while the remaining population is considered back streaming. Moments such as the density or velocity are then computed separately for each population. The method used to separate the core from the back streaming part of the velocity distribution is correct as long as the back streaming components have velocities higher than the set separation radius. This is the case in large areas of the foreshock within several R_E of the foreshock edge where fast field-aligned beam populations are seen [Kempfer *et al.*, 2015]. Deeper in the foreshock, wave-particle interactions perturb more strongly the back streaming populations. In such cases, parts of the back streaming population can be within the separation. Nevertheless, in the areas of interest to the following analysis, the error thus introduced is within 10%, which does not affect the results presented.

Figures 12a and 12b show that the wavefront is born upstream roughly perpendicular to the magnetic field. As the wave advects with the solar wind flow toward the bow shock (Figures 12c–12f), different parts of it encounter plasma with a slower and more dilute beam, making the front oblique close to the foreshock edge.

Figures 12c and 12d show that the part of the wavefront closest to the foreshock edge, where the beam density and velocity are larger than in the central foreshock, is bent, while the wavefront in the central foreshock is less bent. Figures 12e and 12f show that as the wavefront gets closer to the bow shock, it is extended through a variety of beam densities and velocities, making the wavefront more oblique also in the central part of the foreshock.

According to the dispersion relation of the wave, different parts of the wavefront will have a different k . This suggests that refraction may play a role in the bending of the wavefronts also in the radial case that has previously been thought of as a special case where the *Hada et al.* [1987] refraction mechanism has not been thought to operate. Indeed, the *Hada et al.* [1987] mechanism concerns larger cone angles, where the spatial variation of the beam population is caused both by the variation in reflection from the bow shock and the $\mathbf{E} \times \mathbf{B}$ drift that leads to variations in the beam structure. In this paper, the influence of the $\mathbf{E} \times \mathbf{B}$ drift is small, and the variation in the beam density and velocity is caused by the large-scale structure of the foreshock, where in general the highest beam densities and velocities are found at the edges of the foreshock and near the bow shock surface. The quantitative analysis of the beam plasma dispersion relation and its effects on wave refraction in the foreshock will be the subject of a forthcoming study; however, here we can conclude that the wave oblique propagation is due to the variability in the beam density and velocity affecting the refractive index. The highest beam velocities near the foreshock edges are due to a better reflection angle (θ_{bn}) and the fact that there the reflected particles can propagate more easily without being scattered by the ULF waves, while in the central foreshock the beam particles are subjected to wave-particle interactions that modify the beam properties and decelerate the beam particles.

A clear change in the wave propagation angles appears at backbones or spines originating from the bow shock approximately at $Y = -12$ and $2R_E$ (see Figure 1), although their places vary in the run. Similar spines are observed in our other runs and also with coarser resolution (not shown). They are most prominent in the radial geometry but can be identified also with other IMF orientations; and hence, we interpret that they are physical and not of numerical origin. Although such spines have not been reported before explicitly, in Figure 1 of *Blanco-Cano et al.* [2009], global wave break points are visible such that foreshock edge waves have a different propagation angle compared to the central foreshock. These wave break points are quite subtle, which might be a consequence of the number of particles in the simulation of *Blanco-Cano et al.* [2009]. The Vlasov method, due to its continuous and uniform representation of phase space by construction, is somewhat more advantageous in modeling beam-driven wave instabilities and in resolving velocity distributions with both low-density and high-density regions. While similar phase space resolution can be achieved in PIC simulations by, e.g., introducing particle splitting, this introduces another variable into evaluating the correctness of PIC simulations, as the ideal number of particles introduced in a splitting event changes according to the physics involved. In the case of *Blanco-Cano et al.* [2009], Maxwellian particles were split to 16 solar wind particles, indicating that the mass ratio of Maxwellian versus back streaming particles is 1/16. Typically, Vlasiator's ratio is several magnitudes larger. While this kind of rough density estimate does not provide conclusive evidence in comparing the results with *Blanco-Cano et al.* [2009], it does indicate a possible explanation for the discrepancy.

To investigate the nature of the spines, we highlight their approximate positions as dashed white lines in Figure 12. Figure 12 indicates that at the spine location approximately at $Y = 2R_E$ at these time instants, there is a sinusoidal-like back streaming beam with enhanced density moving slowly relative to its surroundings. To investigate the spines in time, we present as a supporting information the movie S2 showing the velocity of the reflected particles. In this movie, it is evident that two processes are behind the spines. First, there are transient preferential places of reflection at the bow shock, from which denser beams are emitted. Through a denser beam, the refractive index would change considerably, which would make the wavefronts bend. Second, there is a global structure in the foreshock, in which the waves are more easily growing and propagating at the foreshock edges, where the density and velocity of the back streaming population is higher. In the central foreshock, the beams travel slower due to the enhanced scattering by the waves and due to less efficient reflection [see also *Kempf et al.*, 2015]. Therefore, there is a global variability in the wave propagation between the edges and the central foreshock, leading to a wave interference approximately at the spine location. This kind of global structure in the foreshock wave field has naturally not been observed, since it would require multiple spacecraft around the foreshock and fortuitous solar wind conditions.

The large-scale structure of the foreshock beam density and velocity also determines the variability of the wave period within the foreshock. The dispersion relation in equation (1) indicates that the wave period and wavelength should be inversely proportional to the beam velocity. Indeed, by looking at the dusk foreshock in Figure 12 and the wave period against the distance from the duskside bow shock in Figure 5 (red dots), we observe that the wave period increases roughly with decreasing beam speed. Similarly, in the vicinity of the bow shock where the beam speed is larger, the wavelength is smaller (Figure 6), again in line with the dispersion relation.

In conclusion, we find that the variability of the back streaming beam density and velocity determines the large-scale structure of the foreshock, which affects the wave frequency, wavelength, and oblique propagation. For observational studies, we predict that the wave propagation angle should be larger in the vicinity of the foreshock edge and smaller far upstream, and that it would depend heavily on the gradient in the beam density and velocity. Similarly, we predict that the foreshock distribution function shapes should correspond to the spatial variations of the beam density and velocity that may be caused by optimal reflection sites from the bow shock or by global wave interference through the foreshock.

Acknowledgments

Vlasiator (<http://vlasiator.fmi.fi>) was developed with the European Research Council Starting grant (200141-QuESpace) granted to M.P. in 2007. The Academy of Finland has also supported the Vlasiator development. We gratefully acknowledge CSC-IT Center for Science for granting us pilot usage of the Sisu super-computer. Vistl [Childs et al., 2012] is used to visualize Vlasiator data. The work at FMI is supported by the Academy of Finland grants 138599 and 267144. Work at ICL is supported by STFC grant ST/K001051/1. U.G. is supported by the German Research Foundation (DFG) grant GA 1968/1. Vlasiator data policy is described in <http://vlasiator.fmi.fi/rules.php>, THEMIS observations and software are fully accessible to the research community (see <http://themis.igpp.ucla.edu>). The OMNI data were obtained from the GSFC/SPDF OMNIWeb interface at <http://omniweb.gsfc.nasa.gov>.

References

- Angelopoulos, V. (2008), The THEMIS mission, *Space Sci. Rev.*, *141*, 5–34, doi:10.1007/s11214-008-9336-1.
- Archer, M., T. S. Horbury, E. A. Lucek, C. Mazelle, A. Balogh, and I. Dandouras (2005), Size and shape of ULF waves in the terrestrial foreshock, *J. Geophys. Res.*, *110*, A05208, doi:10.1029/2004JA010791.
- Auster, H. U., et al. (2008), The THEMIS fluxgate magnetometer, *Space Sci. Rev.*, *141*, 235–264, doi:10.1007/s11214-008-9365-9.
- Bieber, J. W., and E. C. Stone (1979), Energetic electron bursts in the magnetopause electron layer and in interplanetary space, in *Proceedings of Magnetospheric Boundary Layers Conference*, vol. ESA SP-148, pp. 131–135, European Space Agency, Paris.
- Blanco-Cano, X., N. Omid, and C. T. Russell (2006), Macrostructure of collisionless bow shocks: 2. ULF waves in the foreshock and magnetosheath, *J. Geophys. Res.*, *111*, A10205, doi:10.1029/2005JA011421.
- Blanco-Cano, X., N. Omid, and C. T. Russell (2009), Global hybrid simulations: Foreshock waves and cavitons under radial interplanetary magnetic field geometry, *J. Geophys. Res.*, *114*, A01216, doi:10.1029/2008JA013406.
- Blanco-Cano, X., P. Kajdič, N. Omid, and C. T. Russell (2011), Foreshock cavitons for different interplanetary magnetic field geometries: Simulations and observations, *J. Geophys. Res.*, *116*, A09101, doi:10.1029/2010JA016413.
- Childs, H., et al. (2012), Vistl: An end-user tool for visualizing and analyzing very large data, in *High Performance Visualization—Enabling Extreme-Scale Scientific Insight*, 1st edn., vol. 1, pp. 357–372, Taylor and Francis, Boca Raton.
- Eastwood, J. P., A. Balogh, M. W. Dunlop, T. S. Horbury, and I. Dandouras (2002), Cluster observations of fast magnetosonic waves in the terrestrial foreshock, *Geophys. Res. Lett.*, *29*(22), 2046, doi:10.1029/2002GL015582.
- Eastwood, J. P., A. Balogh, C. Mazelle, I. Dandouras, and H. Rème (2004), Oblique propagation of 30 s period fast magnetosonic foreshock waves: A Cluster case study, *Geophys. Res. Lett.*, *31*, L04804, doi:10.1029/2003GL018897.
- Eastwood, J. P., A. Balogh, E. A. Lucek, C. Mazelle, and I. Dandouras (2005a), Quasi-monochromatic ULF foreshock waves as observed by the four-spacecraft Cluster mission: 1. Statistical properties, *J. Geophys. Res.*, *110*, A11219, doi:10.1029/2004JA010617.
- Eastwood, J. P., A. Balogh, E. A. Lucek, C. Mazelle, and I. Dandouras (2005b), Quasi-monochromatic ULF foreshock waves as observed by the four-spacecraft Cluster mission: 2. Oblique propagation, *J. Geophys. Res.*, *110*, A11220, doi:10.1029/2004JA010618.
- Fairfield, D. H. (1969), Bow shock associated waves observed in the far upstream interplanetary medium, *J. Geophys. Res.*, *74*(14), 3541–3553, doi:10.1029/JA074i014p03541.
- Fuselier, S. A., M. F. Thomsen, J. T. Gosling, S. J. Bame, and C. T. Russell (1986), Gyration and intermediate ion distributions upstream from the Earth's bow shock, *J. Geophys. Res.*, *91*(A1), 91–99, doi:10.1029/JA091iA01p00091.
- Gary, S. P. (1993), *Theory of Space Plasma Microinstabilities*, Cambridge Univ. Press, New York.
- Greenstadt, E. W., I. M. Green, G. T. Inouye, A. J. Hundhausen, S. J. Bame, and I. B. Strong (1968), Correlated magnetic field and plasma observations of the Earth's bow shock, *J. Geophys. Res.*, *73*(1), 51–60, doi:10.1029/JA073i001p00051.
- Greenstadt, E. W., G. Le, and R. J. Strangeway (1995), ULF waves in the foreshock, *Adv. Space Res.*, *15*, 71–84.
- Hada, T., C. F. Kennel, and T. Terasawa (1987), Excitation of compressional waves and the formation of shocklets in the Earth's foreshock, *J. Geophys. Res.*, *92*(A5), 4423–4435, doi:10.1029/JA092iA05p04423.
- Hoppe, M. M., and C. T. Russell (1983), Plasma rest frame frequencies and polarizations of the low-frequency upstream waves: ISEE 1 and 2 observations, *J. Geophys. Res.*, *88*, 2021–2028.
- Hoppe, M. M., C. T. Russell, L. A. Frank, T. E. Eastman, and E. W. Greenstadt (1981), Upstream hydromagnetic waves and their association with backstreaming ion populations – ISEE 1 and 2 observations, *J. Geophys. Res.*, *86*, 4471–4492, doi:10.1029/JA086iA06p04471.
- Hsieh, W.-C., and J.-H. Shue (2013), Dependence of the oblique propagation of ULF foreshock waves on solar wind parameters, *J. Geophys. Res. Space Physics*, *118*, 4151–4160, doi:10.1002/jgra.50225.
- Janhunen, P., M. Palmroth, T. V. Laitinen, I. Honkonen, L. Juusola, G. Facsó, and T. I. Pulkkinen (2012), The GUMICS-4 global MHD magnetosphere-ionosphere coupling simulation, *J. Atm. Solar Terr. Phys.*, *80*, 48–59, doi:10.1016/j.jastp.2012.03.006.
- Karimabadi, H., et al. (2014), The link between shocks, turbulence, and magnetic reconnection in collisionless plasmas, *Phys. Plasmas*, *21*, 062308, doi:10.1063/1.4882875.
- Kempf, Y., D. Pokhotelov, S. von Alfthan, A. Vaivads, M. Palmroth, and H. E. J. Koskinen (2013), Wave dispersion in the hybrid-Vlasov model: Verification of Vlasiator, *Phys. Plasmas*, *20*, doi:10.1063/1.4835315.
- Kempf, Y., D. Pokhotelov, O. Gutynska, L. B. Wilson III, B. M. Walsh, S. von Alfthan, O. Hannuksela, D. G. Sibeck, and M. Palmroth (2015), Ion distributions in the Earth's foreshock: Hybrid-Vlasov simulation and THEMIS observations, *J. Geophys. Res. Space Physics*, *120*, doi:10.1002/2014JA020519.
- Killen, K., N. Omid, D. Krauss-Varban, and H. Karimabadi (1995), Linear and nonlinear properties of ULF waves driven by ring-beam distribution functions, *J. Geophys. Res.*, *100*, 5835–5852, doi:10.1029/94JA02899.

- Le, G., and C. T. Russell (1994), The morphology of ULF waves in the Earth's foreshock, in solar wind sources of magnetospheric ultra-low-frequency waves, in *Geophysical Monograph*, vol. 81, edited by M. J. Engebretson, K. Takahashi, and M. Scholer, pp. 81–98, AGU, Washington D. C.
- Mazelle, C., et al. (2003), Production of gyrating ions from nonlinear wave-particle interaction upstream from the Earth's bow shock: A case study from Cluster-CIS, *Planet Space Sci.*, *51*, 785–795.
- McFadden, J. P., C. W. Carlson, D. Larson, V. Angelopoulos, M. Ludlam, R. Abiad, B. Elliott, P. Turin, and M. Marckwordt (2008), The THEMIS ESA plasma instrument and in-flight calibration, *Space Sci. Rev.*, *141*(1–4), 277–302, doi:10.1007/s11214-008-9440-2.
- Meziane, K., C. Mazelle, R. P. Lin, D. LeQuéau, D. E. Larson, G. K. Parks, and R. P. Lepping (2001), Three-dimensional observations of gyrating ion distributions far upstream from the Earth's bow shock and their association with low-frequency waves, *J. Geophys. Res.*, *106*(A4), 5731–5742, doi:10.1029/2000JA900079.
- Meziane, K., et al. (2004), Bow shock specularly reflected ions in the presence of low-frequency electromagnetic waves: A case study, *Ann. Geophys.*, *22*, 2325–2335, doi:10.5194/angeo-22-2325-2004.
- Omidi, N., X. H. Karimabadi, D. Krauss-Varban, and K. Killen (1994), Generation and nonlinear evolution of oblique magnetosonic waves: Application to foreshock and comets, in *Solar System Plasma Physics: Resolution of Processes in Space and Time*, vol. 84, edited by J. L. Burch, pp. 71–84, Geophys. Monogr. Ser., AGU, Washington, D. C.
- Omidi, N., X. Blanco-Cano, and C. T. Russell (2005), Macrostructure of collisionless bow shocks: 1. Scale lengths, *J. Geophys. Res.*, *110*, A12212, doi:10.1029/2005JA011169.
- Omidi, N., D. G. Sibeck, and X. Blanco-Cano (2009), Foreshock compressional boundary, *J. Geophys. Res.*, *114*, A08205, doi:10.1029/2008JA013950.
- Paschmann, G., N. N. Sckopke, J. R. Asbridge, S. J. Bame, and J. T. Gosling (1980), Energization of solar wind ions by reflection from the Earth's bow shock, *J. Geophys. Res.*, *85*, 4689–4693.
- Paschmann, G., N. N. Sckopke, I. Papamastorakis, J. R. Asbridge, S. J. Bame, and J. T. Gosling (1981), Characteristics of reflected and diffuse ions upstream from the Earth's bow shock, *J. Geophys. Res.*, *86*, 4355–4364.
- Palmroth, M., I. Honkonen, A. Sandroos, Y. Kempf, S. von Alfthan, and D. Pokhotelov (2013), Preliminary testing of global hybrid-Vlasov simulation: Magnetosheath and cusps under northward interplanetary magnetic field, *J. Atmos. Solar Terr. Phys.*, *99*, 41–46, doi:10.1016/j.jastp.2012.09.013.
- Pokhotelov, D., S. von Alfthan, Y. Kempf, R. Vainio, H. E. J. Koskinen, and M. Palmroth (2013), Ion distributions upstream and downstream of the Earth's bow shock: First results from Vlsiator, *Ann. Geophys.*, *31*, 2207–2212, doi:10.5194/angeo-31-2207-2013.
- Rojas-Castillo, D., X. Blanco-Cano, P. Kajdič, and N. Omidi (2013), Foreshock compressional boundaries observed by Cluster, *J. Geophys. Res. Space Physics*, *118*, 698–715, doi:10.1029/2011JA017385.
- Russell, C. T., and M. M. Hoppe (1983), Upstream waves and particles, *Space Sci. Rev.*, *34*, 155–172.
- Russell, C. T., J. G. Luhmann, R. C. Elphic, D. J. Southwood, M. F. Smith, and A. D. Johnstone (1987), Upstream waves simultaneously observed by ISEE and UKS, *J. Geophys. Res.*, *92*, 7354–7362.
- Sibeck, D. G., N. Omidi, I. Dandouras, and E. A. Lucek (2008), On the edge of the foreshock: Model-data comparisons, *Ann. Geophys.*, *26*, 1539–1544.
- Takahashi, K., R. L. McPherron, and T. Terasawa (1984), Dependence of the spectrum of Pc 3–4 pulsations on the interplanetary magnetic field, *J. Geophys. Res.*, *89*, 2770–2780.
- von Alfthan, S., D. Pokhotelov, Y. Kempf, S. Hoilijoki, I. Honkonen, A. Sandroos, and M. Palmroth (2014), Vlsiator: First global hybrid-Vlasov simulations of Earth's foreshock and magnetosheath, *J. Atmos. Solar Terr. Phys.*, *120*, 24–35, doi:10.1016/j.jastp.2014.08.012.
- White, L., and A. Adcroft (2008), A high-order finite volume remapping scheme for nonuniform grids: The piecewise quartic method (PQM), *J. Comp. Phys.*, *227*, 7394–7422, doi:10.1016/j.jcp.2008.04.026.
- Winske, D. (1985), Hybrid simulation codes with application to shocks and upstream waves, *Space Sci. Rev.*, *42*, 53–66.
- Winske, D., C. S. Wu, Y. Y. Li, Z. Z. Mou, and S. Y. Guo (1985), Coupling of newborn ions to the solar wind by electromagnetic instabilities and their interaction with the bow shock, *J. Geophys. Res.*, *90*, 2713–2726.
- Zerroukat, M., and T. Allen (2012), A three-dimensional monotone and conservative semi-Lagrangian scheme (SLICE-3D) for transport problems, *Q.J.R. Meteorol. Soc.*, *138*, 1640–1651, doi:10.1002/qj.1902.